DOI: 10.13009/EUCASS2025-313
11TH EUROPEAN CONFERENCE FOR AERONAUTICS AND SPACE SCIENCES (EUCASS)

Aeroacoustic characterization of grid fins in a flight demonstrator

Claudio Marongiu[1†], Lorenzo Beretta[1], Fabio Paglia[1], Alessandro Di Marco[2], Elisa De Paola[2], Luana G. Stoica[2], Matteo Bernardini[3]. Fulvio Stella[3], Piero Pantaleone[4], Salvatore Paiano[4], Davide Franco[4], Corneliu Stoica[5] and Agostino Neri[6]

[1] AVIO S.p.A.,

Via Ariana km 5.2, 00034 Colleferro, Rome, Italy

[2] Department of Civil, Computer Science and Aeronautical Technology Engineering,

Via V. Volterra 62, 00146, Rome, Italy

[3] Department of Aerospace Engineering, University of Rome "La Sapienza"

Via Eudossiana 18, 00184 Rome, Italy

[4]TekRevolution, Via Ex Aeroporto snc- Consorzio il Sole, 80038 Pomigliano d'Arco (Na)

Via Eudossiana 18, 00184 Rome, Italy

[5]INCAS - Institutul Național de Cercetare-Dezvoltare Aerospațială "Elie Carafoli", (Bucarest), Romania

[6]ESA Technical Assistance to Italian PNRR STS Programme, ESA/ESRIN. AIAA Associate Fellow, Frascati (RM) Italy

claudio.marongiu@avio.com - lorenzo.beretta@avio.com - fabio.paglia@avio.com - alessandro.dimarco@uniroma3.it - elisa.depaola@uniroma3.it - luana.stoica@uniroma3.it - matteo.bernardini@uniroma1.it - fulvio.stella@uniroma1.it - p.pantaleone@tekrevolution.it - s.paiano@tekrevolution.it - d.franco@tekrevolution.it - stoica.cornel@incas.ro - agostino.neri@esa.int

[†] Corresponding Author

Abstract

The aerodynamic and aeroacoustic environment of a single stage Flight Demonstrator has been investigated in the frame of the PNRR Space Transportation System Program led by ESA. The flight demonstrator is designed to perform a controlled re-entry phase by deploying a set of four grid fins. Aerodynamic and aeroacoustic impacts in the descent phase have been assessed using wind tunnel testing in different regimes and conditions. Large Eddy Simulations have been also performed to analyze the details of the aerodynamic noise around the vehicle. Results show a very good agreement both in terms of frequency and power spectra distributions.

1. Introduction

The aerodynamic and aeroacoustic environment of a single stage Flight Demonstrator (FD#1), has been evaluated as a part of the activities conducted within the PNRR Space Transportation System (PNRR-STS) program led by ESA [1]. Aim of the program is to demonstrate in flight a number of new technologies properly selected and designed to support the evolution of future green space launch vehicles. The design of a controlled re-entry phase with grid fins deployed is one of the challenges included in the FD#1 mission. The use of the grid fins technology introduces several complexities from the aerodynamic and aeroacoustic standpoint. First appeared around 70's, the grid fins are employed with the scope of improving the aerodynamic stability and controllability of missile configurations. Today, grid fins are largely applied in reusable configurations during descent phases where a more precise control of the re-entry stage is required. Grid fins are non-conventional aerodynamic devices composed by a number of small lifting surfaces arranged in lattice layout and fitted in an external frame. Standard launch vehicle configurations employ four identical grid fins symmetrically located at a specific axial position. Main advantage results to be in the lower hinge moment during the actuation with respect to the ones recorded by traditional wings. Aerodynamics benefits include a better lift and moment characteristics than conventional tail fins, although drag increase in transonic conditions is generally reported as one of the drawbacks [2]. In general, the grid fins enhance the non-linear behaviour of the launch vehicle aerodynamics and, as a consequence, its aeroacoustic impact, especially in the transonic regime [3]. This, among other

DOI: 10.13009/EUCASS2025-313

aspects, justifies the need of a careful aerodynamic assessment, especially during the early phases of a program development as FD#1. The present paper summarizes the activities performed to assess the aerodynamic and aero-acoustic impact in the descent phase of the FD#1 vehicle using the Wind Tunnel (WT) in subsonic, transonic and supersonic regimes at different angles of attack and Reynolds numbers. In parallel, Large Eddy Simulations (LES) have been performed in transonic regime with the scope of analyzing the details of the aerodynamic noise around the vehicle equipped with the grid fins and to offer support to the wind tunnel data interpretation.
The paper is organized as follows. First a section where the WT setup and main results from the experimental campaign are described. A second part reports the output of the LES simulations performed during the test campaign. Last section is dedicated to a critical comparison between experimental data and numerical simulations. A few conclusions of the work are reported at the end of the paper.

2. Wind Tunnel Test Campaign

2.1 Experimental Setup

The Trisonic Wind Tunnel available at INCAS is a blow-down type tunnel [4] that provides air for a short period of time depending on the specified test conditions. The tunnel is capable of testing three speed regimes: subsonic, transonic and supersonic covering a Mach range between 0.4 and 3.5. The Mach number range is achieved by using two separate test sections. The wind tunnel test section has the dimensions of 1.2 x 1.2 m^2 with an interchangeable porous transonic test section with variable porosity from 0.01% to 9%. The transonic test section with porous walls operates in the Mach number range between 0.4 to 1.4. A solid wall test section is instead installed to achieve higher Mach numbers. For the present test campaign, the test section was equipped with the porous wall for the transonic tests and with solid wall for the supersonic tests. Several parameters are acquired during the acoustic tests in order to monitor the flow conditions within the wind tunnel. Pressure fluctuations were measured using 22 high quality Kulite XCQ-062 sensors installed on the model. Where possible, the Kulite sensors were arranged in clusters, to measure the information related to the longitudinal cross-spectra and coherence function along the launcher surface. The test matrix was composed by varying the Mach number between 0.5 up to 2, the Angle of Attack (AoA) from 0 to 10 degrees and the roll angle from 0 to 135 degrees. Fluctuating pressure data were acquired at a sampling frequency of 100 kHz for 2.5s.

The FD#1 model (see Figure 1(a) and Figure 1(b)), was fit in the test section supported by a biconical pivoted sting assembly and a translating vertical strut housed in the upstream end of the variable diffuser section. The rear part of the strut was fixed to the diffuser, while the main front part of the strut could be moved up and down by means of a ball lead screw, driven by a hydraulic motor and servo valve. As the strut moves up or down it operates the pitch angle mechanism housed within the strut. In order to perform measure aerodynamic loads, the model was provided with one internal balance with six components. The model scale was chosen so as to make optimal use of the space available inside the wind tunnel and allow to accommodate the instrumentation inside, while maintaining blockage below the recommended limits. The ogive was truncated in order to allow the model mounting on the sting, after evaluating that the aerodynamic impact of the truncated part is negligible. The sting allows to automatically change the pitch angle; roll changes were done manually, whereas the yaw angle was kept constant. Grid fins were fixed with a support to ensure the design position during the test (see Figure 1(c)).

DOI: 10.13009/EUCASS2025-313

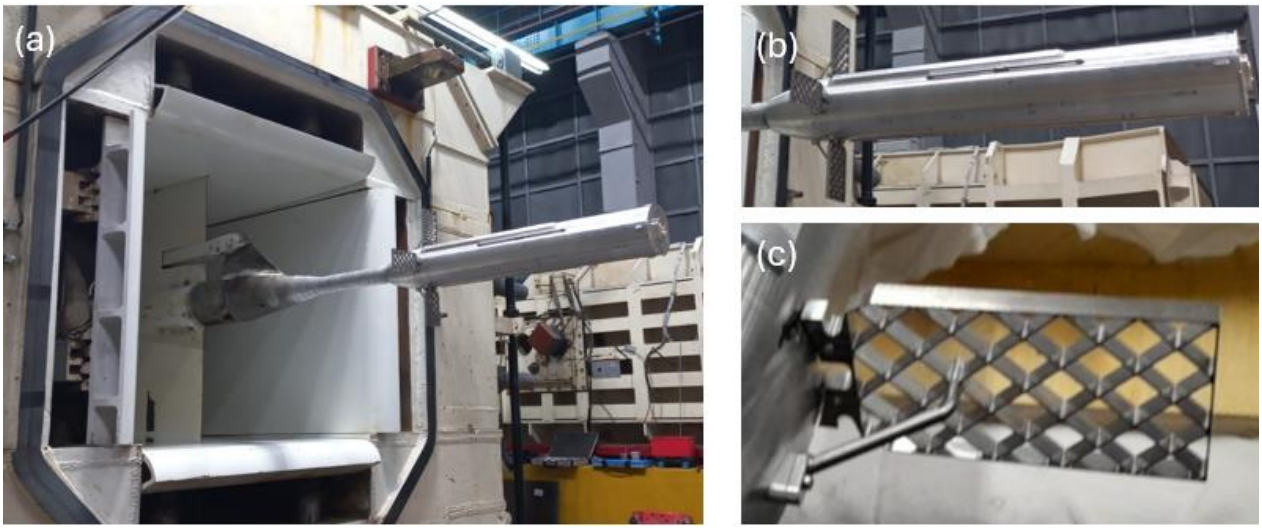

Figure 1. (a) FD#1 model assembly in WT test section; (b) FD#1 model side view; (c) details of the grid fins with the support.

2.2 Experimental measurements

Local flow separations and shock-boundary layer interactions generate large pressure fluctuations occurring mainly in the transonic and low supersonic regimes. Unsteady aerodynamic pressure can excite the vehicle dynamic vibrational modes with the risk of inducing buffeting phenomena. Many investigations on the topic have been carried out since the '60s and a few examples among many are the studies on the Saturn V [6], the Space Shuttle [7], the SLS [8] and [9], the Arianne V [10], the first version of the VEGA launch vehicle [11], and the VEGA-C launch vehicle [12]. Among different objectives, this wind tunnel investigation had the target to clarify whether in transonic flow conditions, tonal excitations were present on the FD#1 model installed within the INCAS WT. The root mean square of the pressure coefficient, $c_{p,rms}$, shows that the amplitudes are in line with previous results (e.g. [13][14][15]). In Figure 2, the $c_{p,rms}$ distributions along the launcher axis are shown at different Mach numbers. The presence of peaks is due to local flow separations that might be induced by wall surface pressure gradients and shock waves. The latter are responsible for thickening the boundary layer and increasing the unsteadiness. Indeed, the pressure transducers where the peaks are located correspond to positions where the flow separation was expected, such as the area located around 30% of the model length from the base, where the numerical simulations predicted the reattachment point after the detachment on the base of the model. A second maximum is measured by the sensor upstream the fin, where a strong bow shock wave occurs, as seen in the Schlieren images (Figure 3), and recirculation can form in front of the grid fin attachment to the body. A decreasing trend of the fluctuating pressure coefficient with the increase in Mach number is noted, as the increased compressibility effects are expected to mitigate pressure fluctuations in the reattachment area.

DOI: 10.13009/EUCASS2025-313

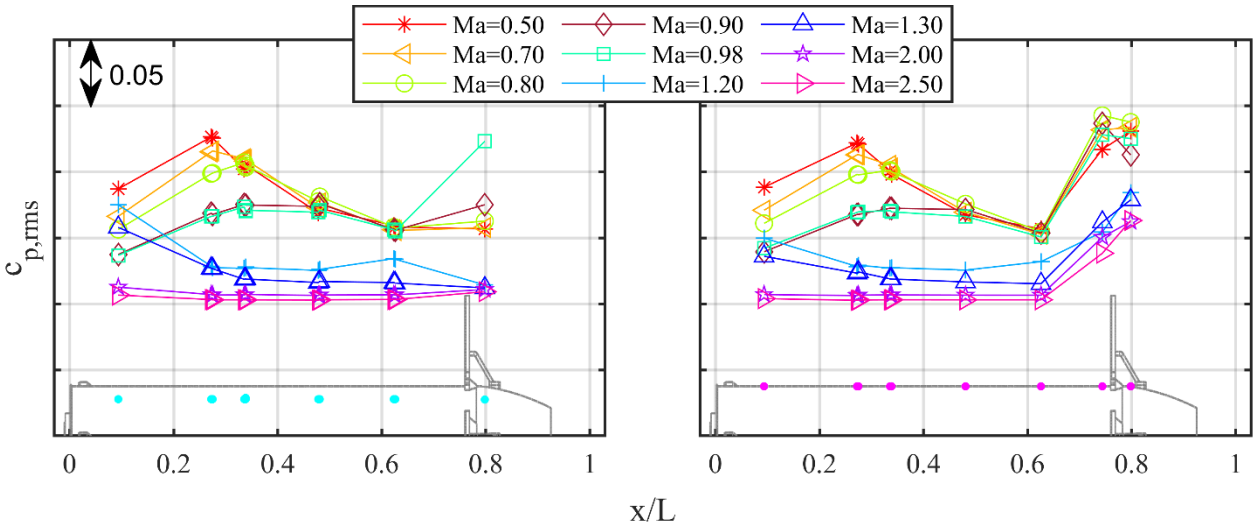

Figure 2. $c_{p,rms}$ evolution along the launcher model at all tested Mach numbers at AoA = 0.

Schlieren images were acquired to detect the shock structures formed on the grid fins in supersonic flow regime at Mach 2 and 2.5. In Figure 3 the images of the shocks formed around the grid fins are clearly visible. An oblique detached bow shock forms upstream the grid fins covering less than half the fin height. In this area, an increase in pressure and a decrease in velocity occurs before entering the grid, increasing the likelihood of choking. On the remaining height of the fins not interacting with the bow shock, shock waves are formed downstream, due to the rapid deceleration of the flow exiting the fin cells, creating sharp pressure discontinuities. Interactions between shocks forming in each cell cause the flow to diverge downstream.

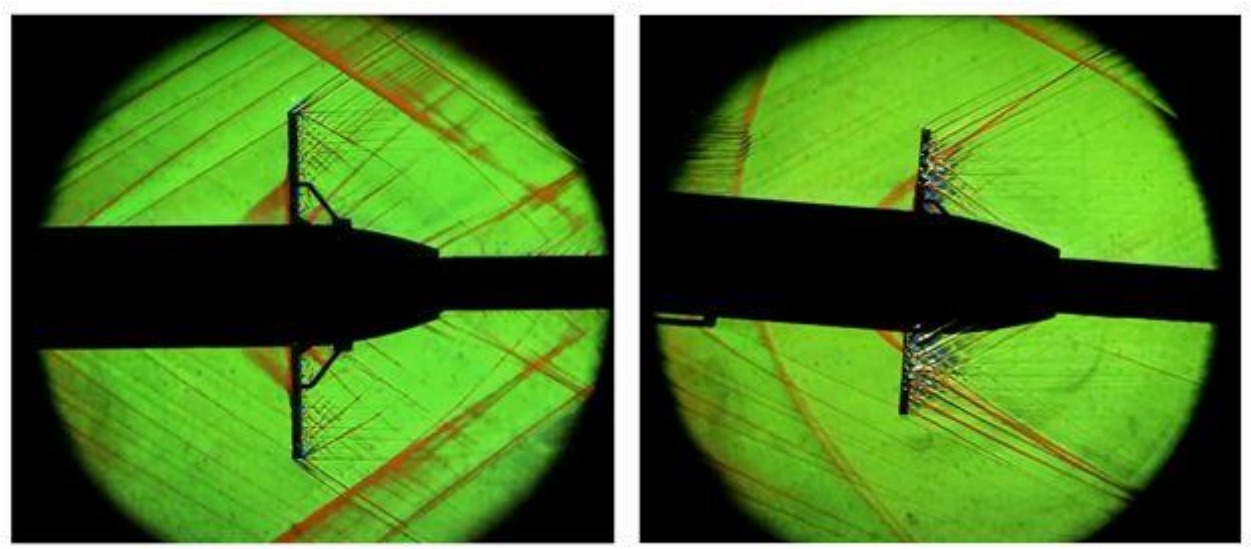

Figure 3. FD#1 Schlieren imaging acquisition in WT. Detail close to the grid fins.

2. Large Eddy Simulation Analyses

2.1 Numerical Method

The numerical prediction of the complex flow field around the FD#1 vehicle, has required the use of high-fidelity computational models capable of effectively handling highly unsteady and separated turbulent flows. As a consequence, turbulence modelling approaches based on the Reynolds-averaged Navier–Stokes (RANS) equations resulted not adequate for the scope. While the Direct Numerical Simulation (DNS) would have been the ideal method

DOI: 10.13009/EUCASS2025-313

to fully capture the sound generation and its propagation, its feasibility for the present Reynolds number applications is still far away because of the huge computational costs. In this context, LES approaches, which directly select the energetically relevant scales of the flow, represent the optimal compromise between accuracy and computational costs. The numerical results discussed in this paper are obtained from the LES of the three-dimensional, compressible, time-dependent Navier–Stokes equations for a perfect and heat-conducting gas. The solver employed is STREAms, Supersonic TuRbulEnt Accelerated Navier–Stokes Solver [16][17]. In contrast to the classical LES, the Implicit Large Eddy Simulation (ILES) approach [18] which STREAms is based upon, consists in an embedded regularization mechanism arising from the discretization of the convective terms. Several studies [19][20] have confirmed that the ILES approach is efficient in utilizing the available grid resolution for capturing the shear-layer transition process while modelling the salient features of the turbulent flow. The numerical method is carefully chosen to provide a physically consistent Sub-Grid Scale (SGS) model. In this context, a number of modifications of the classical Weighted-Essentially Non-Oscillatory (WENO) schemes originally developed by Jiang and Shu [21] have recently appeared [22] which provide lower levels of numerical dissipation maintaining the shock-capturing capabilities of the original schemes. STREAmS solver implements the state-of-the-art of the numerical methods for DNS/LES of high-speed turbulent flows, also in the presence of shock waves. STREAmS is written in Fortran 90, and parallelization is based on a decomposition strategy of the computational domain, which is split in two coordinate directions. Communication between neighbouring blocks is handled by means of Message Passage Interface (MPI) directives that exploit the cartesian topological connectivity. The management of complex geometries relies on the application of an advanced Immersed Boundary Method (IBM) approach, extended to allow the imposition of general boundary conditions. The core of the IBM algorithm implemented in the solver is based on the direct forcing approach, extended to the case of compressible flows in Piquet et al. [23], Bernardini et al. [24]. The computational domain is a large Cartesian box enclosing the FD#1 geometry. Dimensions are adequate to minimize confinement effects and correctly capture the turbulent wake past the vehicle. The final grid selected for the simulations consists of 7424 × 2300 × 2048 nodes (approximately 35 billion points). The grid nodes are stretched in all the coordinate directions towards the launcher geometry to increase the resolution of the immersed boundary method close to the solid body. In particular, the grid spacing is characterized along each coordinate direction by two uniform zones smoothly connected by a hyperbolic tangent function. No-slip, adiabatic boundary conditions are imposed through IBM at the wall, where the Werner Wengle [25] wall function is applied. The analyses focused on post-processing the pressure signals recorded during the simulations and on the computation of the auto-spectra and coherence functions along the vehicle. Numerical simulations have been conducted on the full-scale CAD model of the FD1 vehicle as illustrated Figure 4.

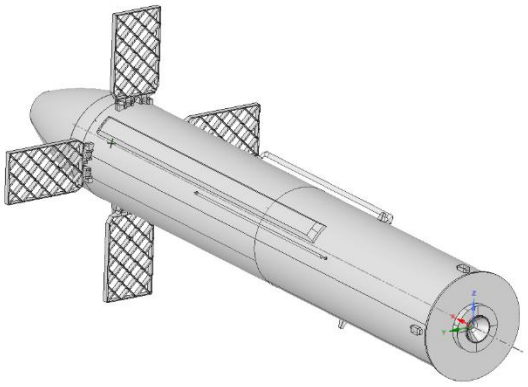

Figure 4. FD#1 CAD Model.

The geometry includes different asymmetric protrusions, such as the Roll Attitude Control Systems (RACS), raceways and external pipes, along with the grid fins, simulated in both in open configurations. The simulations have been performed in transonic conditions considering a specific motor off configuration corresponding to a characteristic point of the designed mission during ascent and descent phase. Main quantities of interest for the characterization of the wall-pressure fluctuations are the Cross Spectral Density function defined as:

$$\boldsymbol{S}_{\boldsymbol{p_a},\boldsymbol{p_b}}(\boldsymbol{\xi},\boldsymbol{\eta},\boldsymbol{f}) = \langle \widetilde{\boldsymbol{p_a}},\, \widetilde{\boldsymbol{p_b}}^{\,*} \rangle \qquad (1)$$

where the brackets denote an ensemble average, $\tilde{p}$ is the Fourier transform of the wall pressure in terms of the frequency f, $\tilde{p}^*$ denotes the complex conjugate of $\tilde{p}$ and the subscripts a and b indicate the position of two arbitrary points on the launcher wall, separated by distances ξ and η in the streamwise and cross-flow direction, respectively. The cross-spectral density is the Fourier transform of the cross-correlation function R:

DOI: 10.13009/EUCASS2025-313

$$\boldsymbol{S_{p_a,p_b}(\xi,\eta,f) = \int_{-\infty}^{+\infty} R_{p_a,p_b}(\xi,\eta,\tau)\, e^{-2\pi f i \tau} d\tau} \quad (2)$$

which can be expressed in non-dimensional form through the coherence function Γ,

$$\Gamma_{p_a,p_b}(\xi,\eta,f) = \frac{\left|S_{p_a,p_b}(\xi,\eta,f)\right|}{S_{p_a,p_b}(\xi,\eta,f)\, S_{p_b,p_a}(\xi,\eta,f)}$$

The coherence function indicates of the strength of the link between the pressure fluctuations at two separate points as a function of the frequency. Indicating with S_{pp} the Power Spectral Density (PSD) for a generic point (and with R_{pp} the corresponding auto-correlation function), the integral over the frequency domain provides the mean square pressure fluctuation:

$$\boldsymbol{p_{rms}^2 = R_{pp}(0) = \int_{-\infty}^{+\infty} S_{pp}(f) df} \quad (3)$$

The corresponding Sound Pressure Level (SPL) defined as

$$\boldsymbol{SPL = 10\, Log_{10}\left(\frac{p_{rms}^2}{p_{ref}^2}\right)} \quad (4)$$

measures the acoustic power relative to a reference value ($p_{ref} = 20\mu$Pa).

2.2 Numerical Results

The salient features of the flow around the FD#1 vehicle are visible in Figure 5, which show the configuration in the ascent and descent phase respectively, in transonic regime and 5° AoA.

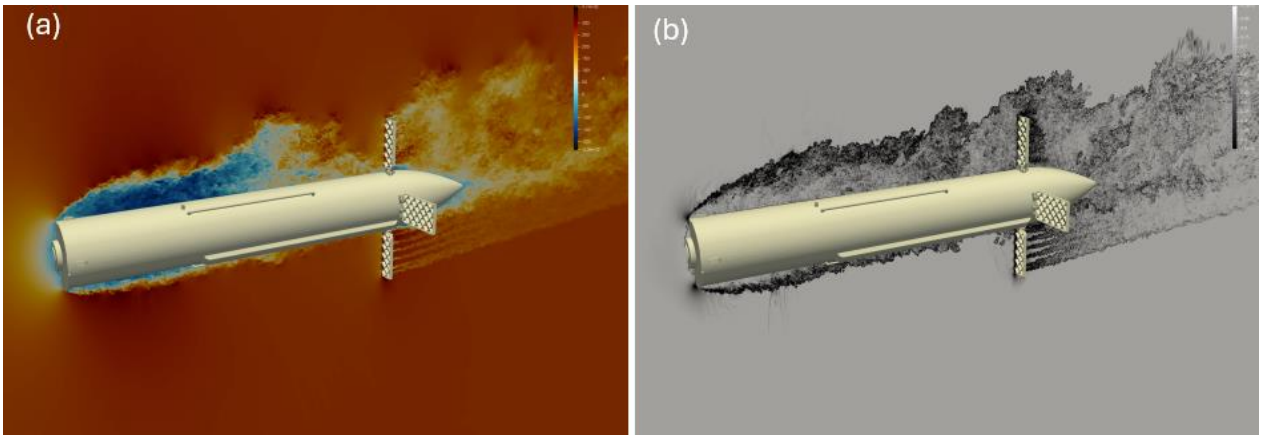

Figure 5. Contours of the instantaneous longitudinal velocity (a) and of the density gradient magnitude (b). LES descent configuration with open grid fins.

During the descent phase after grid fins opening, the boundary layer developing on the vehicle base separates from the base edge becoming a separated shear layer, which starts to roll-up forming vortical structures of different sizes. The separation is not axial-symmetric due to the non-zero AoA which leads to the formation of a large recirculation region on the leeward side, whereas the separation is found to be minimal on the windward side. In the LES solutions, the transition process of the shear layer is fully captured and directly resolved in the energetic, turbulent structures in both the separation region and in the turbulent wake, where classical vortex shedding occurs. The grid fins on the leeward side are invested by a fully turbulent flow as clearly shown by the numerical Schlieren visualization in Figure 5(b),

DOI: 10.13009/EUCASS2025-313

whereas on the windward side the grid fin is exposed to a flow that is mostly irrotational. In the latter case, a pattern of turbulent wakes is observed behind the fins, which later merge proceeding in the downstream direction.

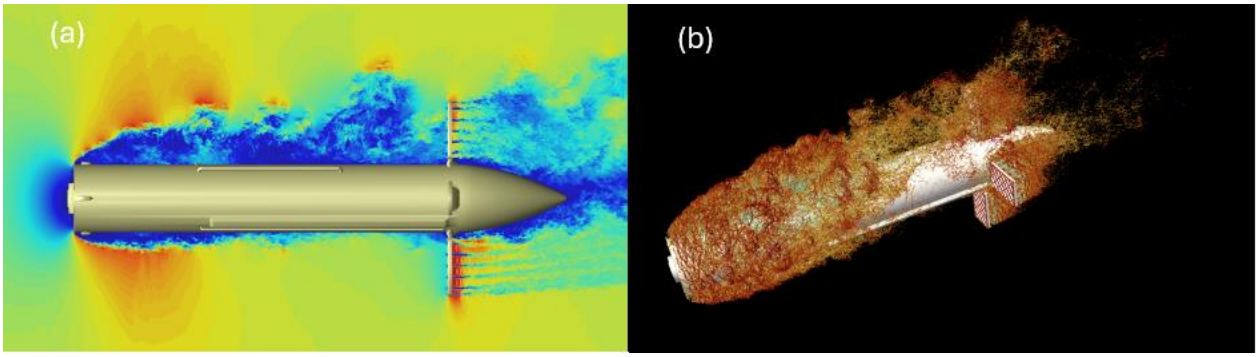

Figure 6. Contours of the instantaneous Mach number field on the central x-z plane (a). Visualisation of the turbulent structures around the FD#1 vehicle by means of the swirling strength criterion (b).

As shown by the contours of the Mach number, reported in Figure 6(a), the flow remains largely subsonic, except for the presence of supersonic bubbles in the first part of the vehicle, on the top of the shear layers and in the zone across the grid fins. In the latter region, the flow expands and through a fluid dynamics throat accelerates up to supersonic velocity before decelerating by means of a series of shock trains that drive the flow to subsonic conditions. A three-dimensional visualization of the turbulent structures captured by LES is reported in Figure 6(b), where an iso-surface of the swirling strength is shown. The figure provides a direct perception of the extremely wide range of scales resolved by the simulation, particularly visible looking at the resolution of the small-scale eddies in the separated regions and in the near wake of the FD#1 vehicle. A global overview of the aeroacoustic loads determined on the FD#1 vehicle can be gained by observing the Figure 7, where the contours of the overall sound pressure level are reported on the whole surface launcher, using different viewpoints. As expected, intense values of the acoustic loads are found towards the center of the launcher where the separated shear layer is expected to reattach, especially on the leeward side. On the other hand, due to the smallest extent of the recirculating region, the windward side is characterized by lower SPL values. However, the highest SPL values are observed on the grid fins, particularly the ones invested by the turbulent flow on the leeward side of the vehicle. On the other grid fins not exposed to the turbulent wakes, the SPL decreases with increasing distance from the launcher body. The frequency content of the wall-pressure signals has been characterized by computing the power spectral density function,

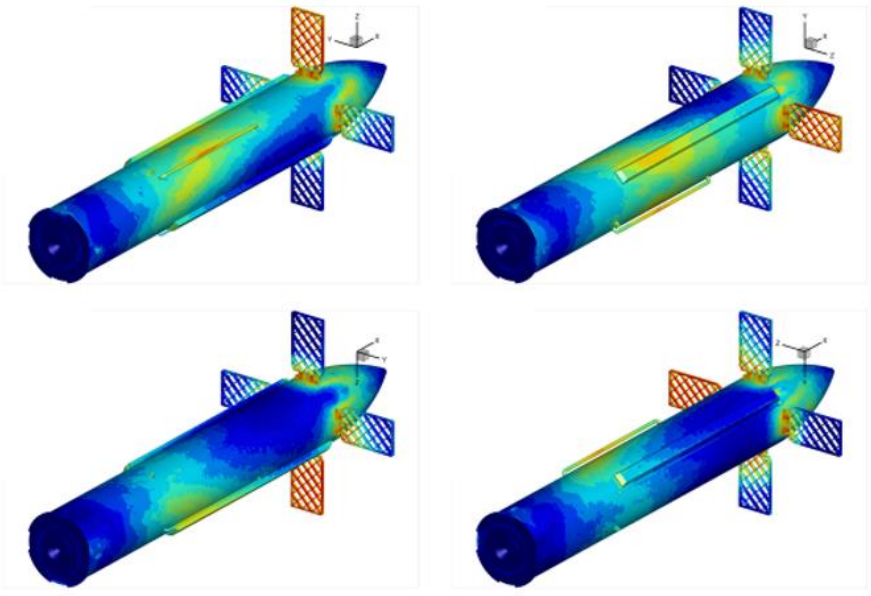

Figure 7. Contours of the overall sound pressure level on the FD#1 vehicle

DOI: 10.13009/EUCASS2025-313

displayed in Figure 8 in the form of two-dimensional maps in the x − f plane, which provide a more complete picture of the spatial distribution of the energy along the longitudinal direction and of the contribution of the different frequencies to the total acoustic loads. On the windward side, as previously observed from the contours of the SPL, the most energetic signals are found towards the fairing and close to the mounting support of the grid fins. The auto-spectra reveal a broadband distribution in the frequency range, with maximum values associated to intermediate frequencies corresponding to a Strouhal number based on the vehicle diameter D equal to St = f D/Vinf ≈ 0.626. A rather different scenario characterizes the leeward side. Here, the maximum values of the acoustic loads are observed approximately three meters away from the base, affecting a large region of the FD vehicle. Concerning the frequency content, while pressure fluctuations are still characterized by a rather broadband distribution, the spectra have a clear peak at lower frequencies (St ≈ 0.12 − 0.24), suggesting a slower dynamics associated with the large scale turbulent structure of the massively separated flow region present on this zone of the FD vehicle.

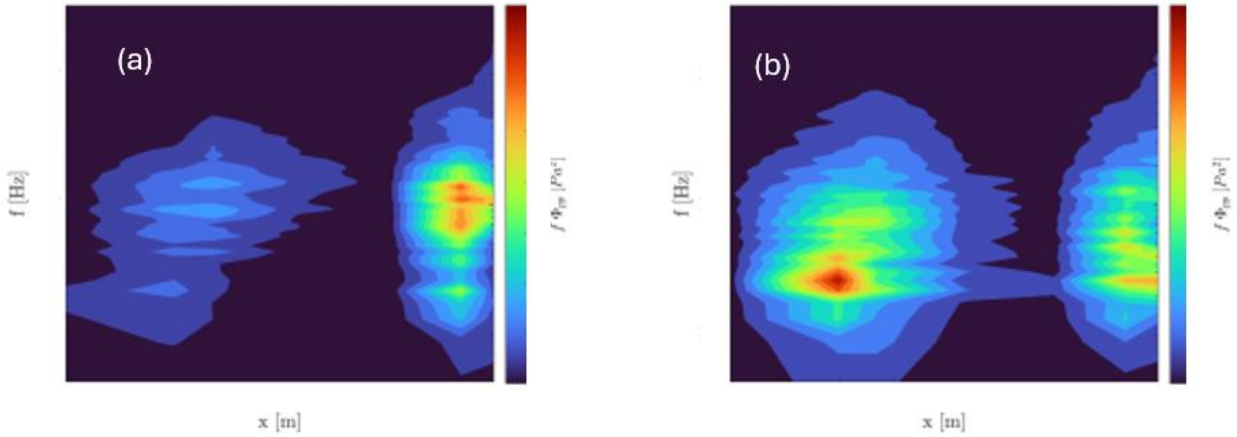

Figure 8. Contours of the pre-multiplied power spectral densities of the wall pressure as a function of the longitudinal coordinate x and frequency f along the launcher, from probes located on the windward side (a) and leeward side (b).

4. Wind Tunnel Test and LES comparisons

Post-test activities have been conducted to assess the results obtained from the WT and LES. Discrepancies between the WTT and LES are in terms the Reynolds number. The experimental Reynolds number achieved in the WT is approximately 4×10^6 , whereas in the LES model it was based on full scale flight conditions (1.2×10^7). The Reynolds number is expected to impact the boundary layer thickness and the dimensions of the recirculation regions. In the LES data, the extension of attached flow downstream the separation, resulted more confined with respect to the experimental observations. This would suggest the presence of a longer separation region on the leeside in the LES data than the one detected in the experiments. Indeed, the numerical and experimental spectra and the $c_{p,rms}$ are far more similar between the sensors in the area downstream the reattachment. Another element of uncertainty to consider is the different turbulence intensity level at the inflow, which resulted higher in the wind tunnel than in the numerical simulations. Further factors examined included the blockage induced by the model although partially compensated by the use of porous wall test section, the flow alignment, namely the effective AoA, and other geometrical variations between the numerical and the experimental models. The impacts of the blockage effect and the inflow turbulent intensity have been considered exploiting the findings in [5], where such effects have been experimentally correlated with pressure fluctuations. Regarding the blockage effects, the formula proposed to compute blockage corrections near separation is:

$$c_{p,rms} = c^0_{p,rms} + 0.8\frac{A}{A_{WT}}$$

Furthermore, a corrective factor to account for the different freestream turbulence level has been introduced as suggested in [5]. Comparisons of the full spectra are made using normalized quantities by dividing by the own variance (σ^2). This method allows to compare the shape of the spectra rather than the different level of the energy content. Results showed in
Figure 9 demonstrate an excellent agreement in terms of sound pressure energy distribution.

DOI: 10.13009/EUCASS2025-313

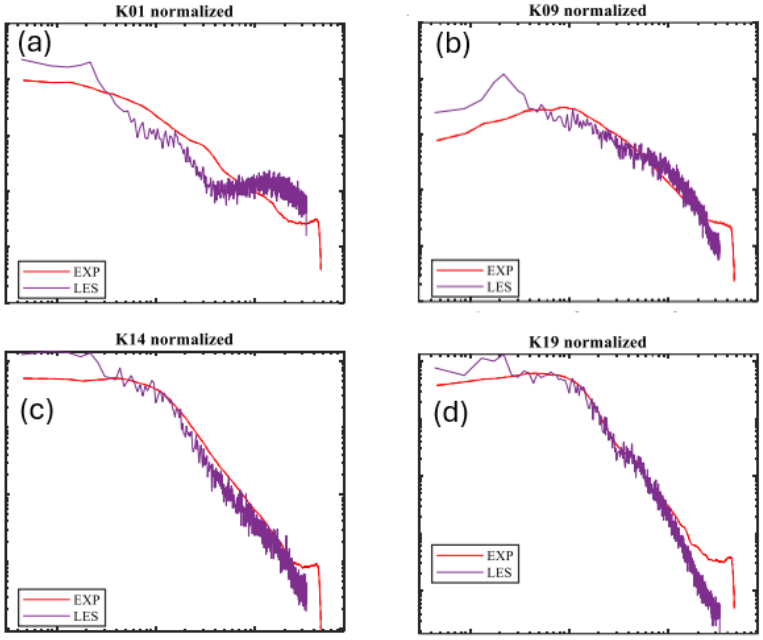

Figure 9. Comparison between the Power Spectra Density from the experimental results and from the LES data for some of the Kulite sensors. K01 and K09 are located along a line not intersecting the grid fins, while K14 and K19 sensors along a line intersecting a grid fin.

The values of the overall SPL are shown in Figure 10, respectively for the sensors on the clean and the grid fins lines respectively. The shape of the OASPL trend along the launcher main axis is well predicted by the LES simulation, with differences from the last sensor close to the grid fin Figure 10(b), which are ascribed to the presence of the fin support not represented in the numerical simulations.

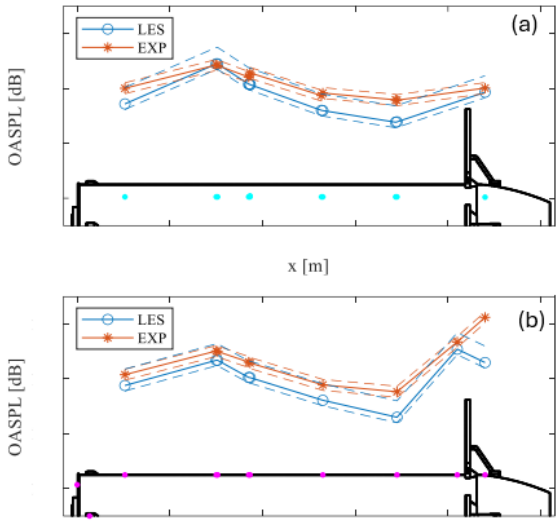

Figure 10. Comparison of the overall SPL between LES and experimental data. Results from the sensors along a line not crossing the grid fin (a), and a crossing line (b).

Coherence functions for a few couples of sensors, in the streamwise, are shown in Figure 11. Different situations occur, depending on the position of the sensors. For the couples reported in Figure 11(a) and Figure 11(b), located on the same azimuth, just downstream the separation point, the shape of the coherence function is quite inconsistent with respect to the LES results, which is also slightly underpredicting the slope. These discrepancies are ascribed to the

DOI: 10.13009/EUCASS2025-313

different evolution of the separation bubble. For couples reported in Figure 11(c) and Figure 11(d), located on the same azimuth on the cylindrical part of the model, an excellent agreement is found between LES and experiments.

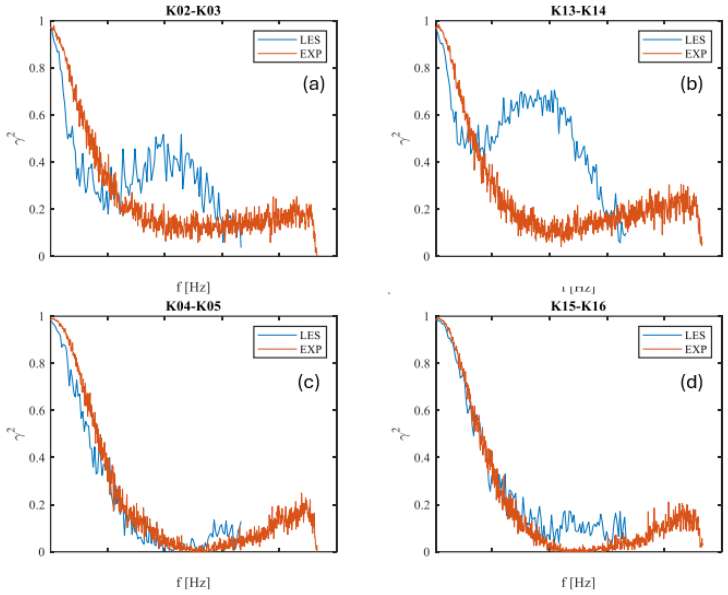

Figure 11. Comparisons between the streamwise coherence functions from the experimental results and the LES data.

5. Conclusions

A test campaign has been conducted on the re-entry single stage configuration launcher vehicle FD#1 equipped with grid fins in deployed configuration. Wind tunnel transonic measurements were conducted to evaluate the unsteady pressure fluctuations acting on the model and compared with high fidelity Large Eddy simulations. Results indicate higher acoustic loads are expected on the leeward side in descent configuration where an extended region of separated flow develops. Aeroacoustic loads are higher for the grid fins invested by the turbulent wakes generated on the leeward side. Detached shock waves are expected to form upstream the grid fins at sufficiently high Mach numbers, leading to increased adverse pressure on part of the fin. Shock waves forming inside the fin cells and the complex interactions among them lead to aerodynamic instability and increased drag. After a post-test correlation activity which considered corrections due to blockage effect and on the free-stream turbulent intensity levels, results show an excellent agreement between the two methodologies in prediction of the sound pressure levels and the frequency contents.

References

[1] Home - Italia Domani - PNRR Portal https://www.italiadomani.gov.it
[2] Theerthamalai, P., Manisekaran, S., and Nagarathinam, M. A Prediction Method for Aerodynamic Characterization of Grid-Fin Configurations at Supersonic Speeds. In: *23rd AIAA Applied Aerodynamics Conference, 6-9 June, 2005*
[3] Munawar S. Analysis of Grid Fins as Efficient Control Surface in comparison to conventional planar fins. In: *27th International Congress of the Aeronautical Sciences ICAS 2010*
[4] Munteanu, Florin. (2009). *INCAS TRISONIC WIND TUNNEL*. *INCAS BULLETIN*. 1. 10.13111/2066-8201.2009.1.1.2.
[5] Saathoff, P. J., & Melbourne, W. H., “Freestream turbulence and wind tunnel blockage effects on streamwise surface pressures”, Journal of Wind Engineering and Industrial Aerodynamics, 26(3), 353- 370, 1987
[6] Jones, G. W., & Foughner, J. T. “Investigation of buffet pressures on models of large manned launch vehicle configurations”, NASA technical note D-1633, 1963
[7] Hanly, R. “Surface-pressure fluctuations associated with aerodynamic noise on the space shuttle launch configuration at transonic and supersonic speeds”, in 17th Structures, Structural Dynamics, and Materials Conference, p. 1527, May 1976

DOI: 10.13009/EUCASS2025-313

[8] Herron, A.J., Crosby, W.A. & Reed, D.K., “Overview of the space launch system ascent aeroacoustic environment test program”, in 54th AIAA Aerospace Sciences Meeting, p. 0543, 2016
[9] Steva, T. B., Pollard, V. J., Herron, A., & Crosby, W. A., ”Space launch system aeroacoustic wind tunnel test results”, in AIAA Aviation 2019 Forum, p. 3303, 2019
[10] Troclet, B., Depuydt, M., & Gonzalez, P., “Experimental analysis of the aerodynamic noise on the Ariane 5 launch vehicle upper part”, in: Conference proceeding ‘‘Ariane 5 structures and technologies,’’ pp.515– 526. France: CNES, 1993
[11] Camussi R., Guj G., Imperatore B., Pizzicaroli A., Perigo D., “Wall pressure fluctuations induced by transonic boundary layers on a launcher model”, Aerospace Science and Technology, 11, pp. 349–359, 2007
[12] Camussi, R. & Di Marco, A., “Aeroacustica Esterna del Lanciatore VEGA C LV - Report”, 14.06.2018
[13] Guj G., Camussi, R., Di Marco, A., Giulietti, A., “Aeroacustica Esterna del Lanciatore VEGA: Caratterizzazione Teorico-Sperimentale”, Contratto di Studio e di Ricerca tra C.I.R.A. e Università Roma Tre, 2003
[14] Panda, J., Garbeff, T. J., Burnside, N. J., & Ross, J. C., “Unsteady pressure fluctuations measured on a hammerhead space vehicle and comparison with Coe and Nute's 1962 data”, International Journal of Aeroacoustics, 17(1–2), pp. 70–87, 2018
[15] Camussi, R. & Di Marco, A., “Aeroacustica Esterna del Lanciatore VEGA C LV - Report”, 14.06.2018
[16] Bernardini, M., Modesti, D., Salvadore, F., & Pirozzoli, S. (2021). STREAmS: A high-fidelity accelerated solver for direct numerical simulation of compressible turbulent flows. Computer Physics Communications, 263, 107906.
[17] Bernardini, M., Modesti, D., Salvadore, F., Sathyanarayana, S., Della Posta, G., & Pirozzoli, S. (2023). STREAmS-2.0: Supersonic turbulent accelerated Navier-Stokes solver version 2.0. In Computer Physics Communications, 285, 108644
[18] Fernando F Grinstein, Len G Margolin, and William J Rider. Implicit large eddy simulation, volume 10. CUP, 2007.
[19] C. Brehm, J. A Housman, and C. C. Kiris. Noise generation mechanisms for a supersonic jet impinging on an inclined plate. Journal of Fluid Mechanics, 797: 802–850, 2016. doi: 10.1017/jfm.2016.244.
[20] [4] Michael L Shur, Philippe R Spalart, and Michael Kh Strelets. Noise prediction for increasingly complex jets. part I: Methods and tests. International Journal of Aeroacoustics, 4(3):213–245, 2005. doi: 10.1260/1475472054771376.
[21] Guang-Shan Jiang and Chi-Wang Shu. Efficient implementation of weighted ENO schemes. Journal of Computational Physics, 126(1):202–228, 1996. doi: 10.1006/ jcph.1996.0130.
[22] Rafael Borges, Monique Carmona, Bruno Costa, and Wai Sun Don. An improved weighted essentially non-oscillatory scheme for hyperbolic conservation laws. Journal of Computational Physics, 227(6):3191–3211, 2008. ISSN 0021-9991. doi: 10.1016/j.jcp.2007.11.038.
[23] A. Piquet, O. Roussel, and A. Hadjadj. A comparative study of Brinkman penalization and direct-forcing immersed boundary methods for compressible viscous flows. Computer and Fluids, 136:272–284, 2016. doi: 10.1016/j.compfluid.2016.06.001
[24] M. Bernardini, D. Modesti, and S. Pirozzoli. On the suitability of the immersed boundary method for the simulation of high-Reynolds-number separated turbulent flows. Computers Fluids, 130:84–93, 2016. ISSN 0045-7930. doi: 10.1016/j. compfluid.2016.02.018
[25] H. Werner and H. Wengle. Large-eddy simulation of turbulent flow over and around a cube in a plate channel. In Turbulent Shear Flows 8, pages 155–168, Berlin, Heidelberg, 1993. Springer Berlin Heidelberg. ISBN 978-3-642-77674-8